PHYSICAL REVIEW MATERIALS **7**, 054005 (2023)

Epitaxial van der Waals heterostructures of Cr_2Te_3 on two-dimensional materials

Quentin Guillet,[1,*] Libor Vojáček,[1,*] Djordje Dosenovic,[2] Fatima Ibrahim,[1] Hervé Boukari,[3] Jing Li,[4] Fadi Choueikani,[5] Philippe Ohresser,[5] Abdelkarim Ouerghi,[6] Florie Mesple,[7] Vincent Renard,[7] Jean-François Jacquot,[8] Denis Jalabert,[2] Hanako Okuno,[2] Mairbek Chshiev,[1,9] Céline Vergnaud,[1] Frédéric Bonell,[1] Alain Marty,[1] and Matthieu Jamet[1]
[1] *Université Grenoble Alpes, CEA, CNRS, IRIG-SPINTEC, 38000 Grenoble, France*
[2] *Université Grenoble Alpes, CEA, IRIG-MEM, 38000 Grenoble, France*
[3] *Université Grenoble Alpes, CNRS, Institut Neel, 38000 Grenoble, France*
[4] *Université Grenoble Alpes, CEA, Leti, 38000 Grenoble, France*
[5] *Synchrotron SOLEIL, L'Orme des Merisiers, 91190 Saint-Aubin, France*
[6] *Université Paris-Saclay, CNRS, Centre de Nanosciences et de Nanotechnologies, Palaiseau, France*
[7] *Université Grenoble Alpes, CEA, CNRS, IRIG-PHELIQS, 38000 Grenoble, France*
[8] *Université Grenoble Alpes, CEA, CNRS, IRIG-SYMMES, 38000 Grenoble, France*
[9] *Institut Universitaire de France, 75231 Paris, France*

(Received 25 February 2023; accepted 28 April 2023; published 16 May 2023)

Achieving large-scale growth of two-dimensional (2D) ferromagnetic materials with high Curie temperature T_C and perpendicular magnetic anisotropy (PMA) is highly desirable for the development of ultracompact magnetic sensors and magnetic memories. In this context, van der Waals (vdW) Cr_2Te_3 appears to be a promising candidate. Bulk Cr_2Te_3 exhibits strong PMA and a T_C of 180 K. Moreover, both PMA and T_C might be adjusted in ultrathin films by engineering composition or strain or applying an electric field. In this work, we demonstrate the molecular beam epitaxy (MBE) growth of vdW heterostructures of five-monolayer quasifreestanding Cr_2Te_3 on three classes of 2D materials: graphene (semimetal), WSe_2 (semiconductor), and Bi_2Te_3 (topological insulator). By combining structural and chemical analysis down to the atomic level with *ab initio* calculations, we confirm the single-crystalline character of Cr_2Te_3 films on the 2D materials with sharp vdW interfaces. They all exhibit PMA and T_C close to the bulk Cr_2Te_3 value of 180 K. *Ab initio* calculations confirm this PMA and show how its strength depends on strain. Finally, Hall measurements reveal a strong anomalous Hall effect, which changes sign at a given temperature. We theoretically explain this effect by a sign change of the Berry phase close to the Fermi level. This transition temperature depends on the 2D material in proximity, notably as a consequence of charge transfer. MBE-grown Cr_2Te_3/2D material bilayers constitute model systems for the further development of spintronic devices combining PMA, large spin-orbit coupling, and sharp vdW interface.

DOI: 10.1103/PhysRevMaterials.7.054005

I. INTRODUCTION

The discovery of ferromagnetic order in two-dimensional (2D) materials like $Cr_2Ge_2Te_6$ [1] and CrI_3 [2] has paved the way for the development of new van der Waals (vdW) heterostructures [3]. Combined with the large spin-orbit coupling and low crystal symmetries of 2D materials like transition metal dichalcogenides [4], 2D ferromagnets represent a key ingredient to construct ultracompact devices for spintronic applications [5] such as spin transfer torque and spin-orbit torque magnetic random access memories. These technologies based on 2D materials would allow for the miniaturization of today's devices as well as a sizable reduction of energy consumption [6].

For this purpose, 2D ferromagnets with Curie temperatures T_C higher than room temperature and with perpendicular magnetic anisotropy (PMA) are required [7]. Fe_xGeTe_2 ($x = 3, 4$, or 5) [8] and $Cr_{1+\delta}Te_2$ ($0 \leqslant \delta \leqslant 1$) [9–23] emerged recently as the two most promising families of materials to achieve such conditions. $Cr_{1+\delta}Te_2$ materials are composed of $1T$-$CrTe_2$ monolayers (ML) separated by a variable number of intercalated chromium atoms (from empty to fully occupied). $CrTe_2$ is a vdW ferromagnet with room temperature ferromagnetic order ($T_C = 315$ K) [9–11], whereas $Cr_{1+\delta}Te_2$ ($\delta > 0$) are quasi-vdW ferromagnets with T_C ranging from 160 to 350 K and varying magnetic anisotropy from the out-of-plane to in-plane easy axis of magnetization [9-14]. Magnetic properties of $Cr_{1+\delta}Te_2$ have been shown to depend on its stoichiometry [12,13], its thickness in the case of thin films [14], the Cr-Te flux ratio during crystal growth [15], and strain in the layer [16,17]. The stoichiometry of the stack could be adjusted by postgrowth annealing [12] or by changing elemental fluxes [18]. Lasek *et al.* [19] showed that for a monolayer of $Cr_{1+\delta}Te_2$, stoichiometry could vary with growth/annealing temperature between $\delta = 0.5$ and 1. Highly efficient control of magnetic properties is required for spintronic applications [5], and it is, therefore, necessary to understand the growth mechanisms of these materials, especially for the development of functional vdW heterostructures. Exotic topological phenomena such as the topological Hall effect have also been reported in Cr_2Te_3/Bi_2Te_3 bilayers

---

[*] These authors contributed equally to this work.

[20,21] and Cr_2Te_3/Cr_2Se_3 [22]. Moreover, noncollinear spin textures were shown in Cr_2Te_3 as a consequence of antiferromagnetic coupling between neighboring chromium atoms [23], making it an interesting host for exotic, trivial, or topological spin textures.

In this work, we report the vdW epitaxy [24,25] of 5 ML of Cr_2Te_3 for three different 2D materials, namely, graphene (a semimetal with exceptional electronic properties), WSe_2 (a transition metal dichalcogenide semiconductor exhibiting strong photoluminescence and spin-valley locking in its monolayer form), and Bi_2Te_3 (a topological insulator with strong spin-orbit interaction). Particular care was given to their full structural and magnetic characterizations, including the determination of the film stoichiometry. Those bilayers represent model systems to study proximity effects in vdW heterostructures, interface spin textures, and spin-orbit torques. The Cr_2Te_3 films were grown by molecular beam epitaxy (MBE) in ultrahigh vacuum (UHV) by simultaneously depositing Cr and Te atoms. They exhibit in-plane compression and out-of-plane expansion with respect to the bulk phase. This strain is shown to vary with the postgrowth annealing, but it is almost independent of the 2D layer underneath. Indeed, Cr_2Te_3 films on graphene and WSe_2 annealed at 400 °C show the same lattice parameters, which are equal to those of 5 ML freestanding Cr_2Te_3 calculated using *ab initio* methods. This demonstrates that the vdW epitaxy of Cr_2Te_3 on 2D materials leads, after annealing, to the formation of quasifreestanding films with negligible interaction with the substrate. We then correlate the PMA of Cr_2Te_3 with strain and confirm our experimental findings using *ab initio* calculations. Finally, magnetotransport measurements reveal a change in sign of the anomalous Hall effect in Cr_2Te_3 with temperature and point out a charge transfer from the substrate to the film, changing the *p*-type doping level of Cr_2Te_3. This effect was already observed in several vdW heterostructures [26,27]. The charge transfer is shown to govern the temperature at which the anomalous Hall effect changes sign. We theoretically reproduce this effect by showing a sign change in the Berry phase close to the Fermi level. Finally, our work demonstrates the ability of MBE to synthesize model vdW heterostructures incorporating 2D materials and quasi-vdW ferromagnets which are highly promising for future 2D-based spintronic devices.

II. METHODS

A. Experimental methods

All the films were grown by MBE using a home-designed UHV system. Metallic elements (Cr, W, Bi, and Al) were evaporated using an electron gun, and the growth rate was controlled using a quartz microbalance, whereas chalcogens (Te, Se) were evaporated from Knudsen cells. Their elemental fluxes were measured by a pressure gauge. The substrates were attached to a molybloc by wetting In underneath. The temperature of the samples during growth was controlled by a thermocouple touching the backside of the molybloc.

Scanning transmission electron microscopy (STEM) measurements were performed using a Cs-corrected FEI Themis at 200 kV. High-angle annular dark field (HAADF) STEM images were acquired using a convergence angle of 20 mrad and collecting electrons scattered at angles higher than 60 mrad. STEM specimens were prepared by the focused ion beam (FIB) lift-out technique using a Zeiss Crossbeam 550. The sample was coated with protective carbon and platinum layers prior to the FIB cut.

The out-of-plane x-ray diffraction (XRD) measurements were performed using a Panalytical Empyrean diffractometer operated at 35 kV and 50 mA, with a cobalt source ($K\alpha = 1.79$ Å). A PIXcel-3D detector allowed a resolution of 0.02° per pixel, in combination with a divergence slit of 0.125° on the source side. Grazing in-plane XRD measurements were performed with a SmartLab Rigaku diffractometer equipped with a copper rotating anode ($K\alpha = 1.54$ Å) operating at 45 kV and 200 mA. Collimators with a resolution of 0.5° were used on both the source and detector sides. The grazing incidence close to the critical angle of the substrate was optimized to maximize the intensity of the Cr_2Te_3 Bragg peaks. Both diffractometers were equipped with multilayer mirrors on the source side and a $K\beta$ filter on the detector side.

Raman measurements were performed with a Horiba Raman setup with a 632 nm laser excitation source and a spot size of 0.5 μm. The signal was collected by using a 1800 grooves/mm grating.

Rutherford backscattering (RBS) measurements were performed with a $^4He^+$ beam delivered by the SAFIR Platform at Sorbonne University in Paris at beam energies ranging from 1.5 to 2.0 MeV. For all samples, the scattering angle was set to 160°, and the resolution of the detector was 13.5 keV. To avoid channeling effects, the samples were tilted with respect to the normal of the sample in two perpendicular directions.

The magnetic properties were measured by superconducting quantum interference device (SQUID) magnetometry with the magnetic field applied parallel or perpendicular to the film plane. The measurements were performed using a Quantum Design magnetic property measurement system. The diamagnetic contribution was subtracted using the data at high field ($\geqslant 3$ T), and some parasitic contributions were corrected by subtracting signals measured well above the T_C of the systems (at 350 K). This method was already used successfully by Ribeiro *et al.* [8] and confirmed by comparing it with magnetic moments extracted from x-ray magnetic circular dichroism (XMCD) measurements. To extract the magnetic anisotropy energy, we calculated the area between the saturation magnetization and the fist magnetization curve for both directions of the applied magnetic field. The magnetic anisotropy energy was then expressed as the difference between the two areas for the field applied in plane and the field applied out of plane.

The XMCD measurements were performed on the DEIMOS beamline [28] of synchrotron SOLEIL (Saint Aubin, France). The signals were recorded using the total electron yield method. Each XMCD spectrum was obtained from four measurements, in which both the circular helicity and the direction of the applied magnetic field were flipped. The XAS data were then averaged (the signals of opposite helicity and field) and normalized to the absorption at the preedge of chromium (565 eV). The XMCD spectra were normalized to their maximum for comparison.

In order to carry out magnetotransport measurements, we processed Hall bars out of Cr_2Te_3 films by laser lithography and argon etching. Electrical contacts were made of *e*-beam evaporated Ti(10 nm)/Au(100 nm) bilayers. The length and width of Hall bars were approximately 100 and 10 μm, respectively. All the electrical measurements were performed using an Oxford Spectromag setup working in the 1.6–300 K temperature range with magnetic fields up to 7 T. The anomalous Hall contribution was obtained by fitting the experimental data with a hyperbolic tangent function.

B. Calculation methods

The *ab initio* calculations were performed using density functional theory (DFT) as implemented in the Vienna *Ab initio* Simulation Package (VASP) [29,30] with the generalized gradient approximation pseudopotentials in the Perdew-Burke-Ernzerhof parametrization [31]. The DFT+U approach using Dudarev's formulation [32] was applied with an effective Hubbard correction $U_{\text{eff}} = 2.1$ eV to localize the Cr d orbitals. A Cr pseudopotential with semicore p electrons was chosen, and an energy cutoff of 330 eV was used for the plane-wave basis. The van der Waals interaction was approximated by the Grimme's dispersion correction in density functional theory (DFT-D3) [33] with the Bescke-Johnson damping [34].

To compute the relaxed heterostructures of Cr_2Te_3 with 2D materials, the relative orientation of the two materials in the calculation was not taken from an experiment but chosen in a systematic way [35] to minimize the lattice mismatch. This captures more realistically the weak epitaxy of the heterostructure.

The magnetic anisotropy energy is calculated as the difference between the ground state free energies when the magnetization points in plane and out of plane [36]. A $9 \times 9 \times 5$ k-point mesh was found to be sufficient. The volume was fixed at its calculated equilibrium bulk value, while the in-plane and out-of-plane lattice parameters (a and c) were varied. A demagnetizing energy contribution $E_{\text{demag}} = -\mu_0 M_s^2/2$ was added to the calculated magnetocrystalline energy, using the experimental M_s value of ≈300 kA/m.

The anomalous Hall effect was computed [37] by constructing a tight-binding Hamiltonian based on maximally localized Wannier functions using the WANNIER90 package [38]. We verified carefully that the model reproduces well the band structure of Cr_2Te_3 from the original DFT calculation. Using the WANNIERBERRI package [39,40], the Berry curvature was then calculated for a dense k-point mesh and integrated over the Brillouin zone to obtain the Berry phase, which is proportional to the anomalous Hall conductivity, at various Fermi level positions.

III. SAMPLE PREPARATION

In this study, we grew samples of five layers of Cr_2Te_3 corresponding to a thickness of 6.1 nm on three different vdW surfaces: 1 ML of WSe_2 deposited on GaAs; 10 layers of Bi_2Te_3 on Al_2O_3, which were both grown *in situ* by MBE; and monolayer graphene, which was obtained by the controlled graphitization of 4*H*-SiC(0001) [41–43] in another reactor.

WSe_2 was grown epitaxially on Se-passivated GaAs(111)B as detailed in [44]. Bi_2Te_3 was grown epitaxially on sapphire. For this purpose, sapphire substrates were first annealed in air for 1 h at 1000 °C with a heating ramp of 40 min starting from room temperature. They were additionally annealed *in situ* for 30 min at 800 °C. Ten quintuple layers of Bi_2Te_3 were then grown by coevaporating Bi and Te from an electron gun and a cracker cell at deposition rates of 0.057 and 0.1 Å/s, respectively. The substrate temperature was maintained at 250 °C during the growth. Postgrowth annealing at 300 °C under Te flux was done for 10 min to improve the crystal quality. Finally, Gr/SiC layers were annealed *in situ* for 30 min at 650 °C after their transfer.

The Cr_2Te_3 films were grown using a two-step process as sketched in Fig. 1(a). The growth temperature, Te:Cr ratio, and deposition rate were set at 300 °C, 10, and 0.25 L/min, respectively. The Te cell shutter was opened 1 min before chromium deposition to ensure that the surface of the substrate was saturated in Te at the first stage of growth [see Fig. 1(a)]. After the growth, the samples were annealed at 400 °C for 10 min using the same Te flux as during the growth and a heating ramp of 40 °C/min. The samples were then cooled down to 50 °C, and 3 nm of aluminum were deposited to prevent oxidation of the layers during transfers between experimental setups.

The film morphology was monitored *in situ* by reflection high-energy electron diffraction (RHEED), as can be seen in Fig. 1(b) in the case of WSe_2. A streaky diffraction pattern was observed, indicating a flat and well-crystallized surface. The different diffraction patterns along the two high-symmetry axes of the WSe_2 substrate [Figs. 1(c), 1(e)] indicate a good alignment of Cr_2Te_3 grains with the underlying layer. After annealing, the width of the diffraction rods is approximately divided by 2 as a consequence of the larger grain size [Figs. 1(d), 1(f)]. We made similar RHEED observations for the two other vdW substrates, Bi_2Te_3 and graphene (see the Supplemental Material [45]), except an increased isotropic contribution on graphene attributed to a lower interaction with the substrate.

IV. STRUCTURAL PROPERTIES

We found similar structural characteristics for Cr_2Te_3 grown on WSe_2 and graphene. Therefore, we present the results for the growth on WSe_2, and the ones for the growth on graphene are given in the Supplemental Material [45]. The results for Bi_2Te_3 are shown in Fig. 5 below.

Figure 2(a) is a cross-section STEM image of the layers, revealing a sharp and well-defined interface between the vdW ferromagnet and the 2D layer, as evidenced by the W-Te distance between W atoms of WSe_2 and the first Te atom plane of Cr_2Te_3 with a value of 5.3 Å. This value is taken to obtain a better experimental determination of the gap (due to the large atomic number of W with respect to Se), as shown in Fig. 2(b) by a line profile along the c direction of the heterostructure. This corresponds to a vdW gap Δc_{vdW} of 3.5 Å if we assume a relaxed WSe_2 layer, in agreement with our XRD data (see Fig. 3). It is worth noting that we resolve an intensity difference in the line profile [Fig. 2(b)] between fully and partially filled Cr planes. Indeed, for every two Cr planes, only one third of the lattice sites are occupied by intercalated Cr atoms in the case of Cr_2Te_3. We also observe that the

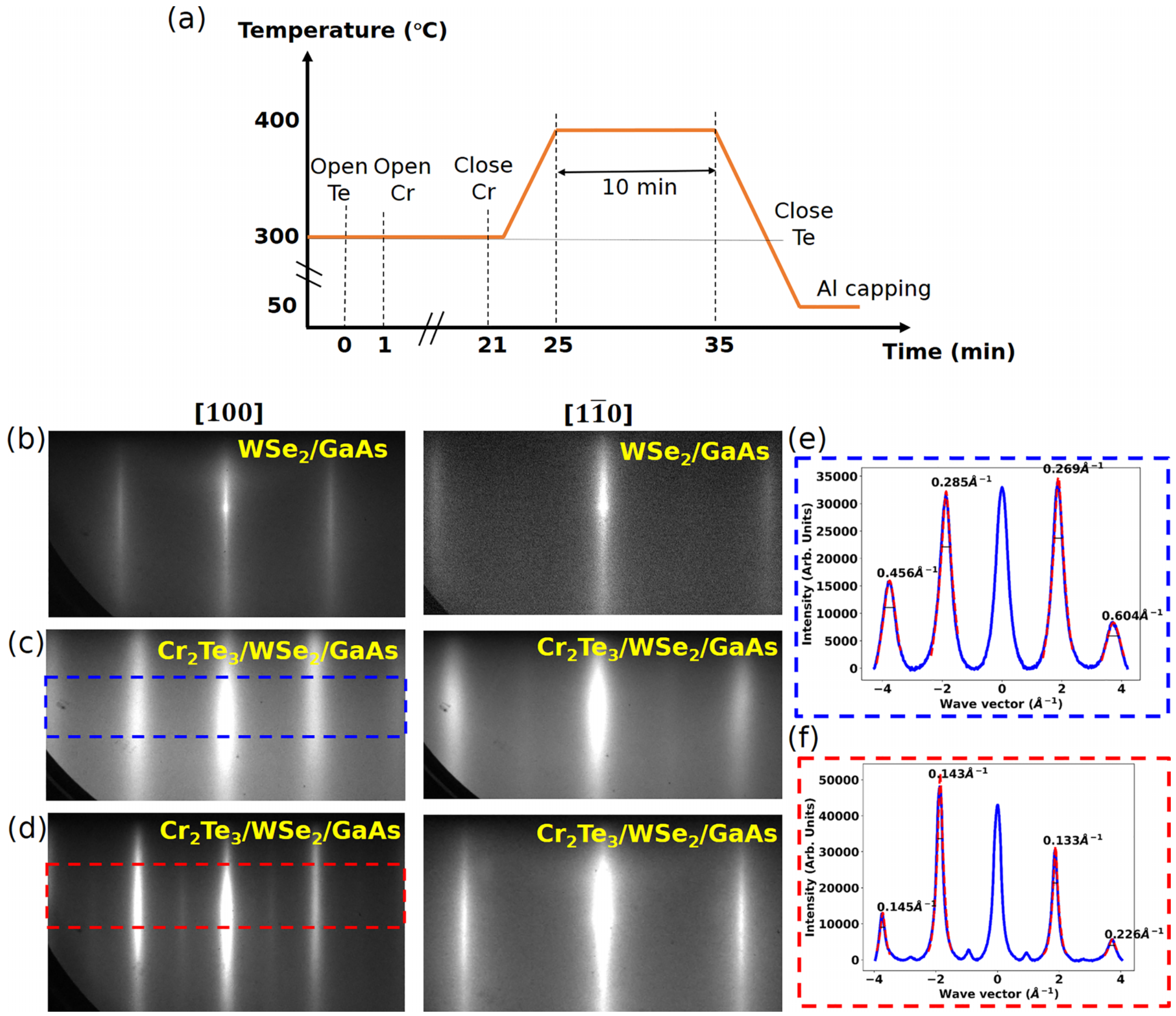

FIG. 1. MBE growth of Cr_2Te_3 on the 2D transition metal dichalcogenide WSe_2. (a) Sketch of the deposition procedure. The growth temperature was 300 °C and *in situ* annealing was performed at 400 °C. (b) *In situ* RHEED images of one-layer WSe_2 deposited on GaAs(111)B along two crystal directions (time = 0 min). (c) RHEED pattern after the deposition of Cr_2Te_3 (time = 21 min). (d) RHEED pattern after annealing (time = 35 min). (e) and (f) Intensity profiles of the RHEED diffraction pattern for (c) (blue dashed box) and (d) (red dashed box), respectively.

monolayer of WSe_2 remains intact after the growth of Cr_2Te_3 on top.

The experimental W-Te distance was compared with the one obtained by *ab initio* calculations performed on Cr_2Te_3/WSe_2 consisting of 1.5 unit cell thick Cr_2Te_3 on top of a single layer of WSe_2 [see Fig. 2(c)]. The calculated distance is 5.08 Å, very close to the experimental value of 5.3 Å.

To accurately determine the lattice parameters of Cr_2Te_3 layers and crystal orientation with respect to each of the substrates, systematic XRD analyses were performed to extract the in-plane and out-of-plane lattice parameters. These measurements allowed us to measure accurately the strain in each layer when compared with the bulk lattice parameters.

Figures 3(a)–3(c) show XRD out-of-plane, in-plane radial, and in-plane azimuthal scans of Cr_2Te_3/WSe_2/GaAs (sample 2; see Table I), respectively. The diffraction patterns of Cr_2Te_3 deposited on WSe_2 reveal the single-crystalline character of the film and the clear epitaxial relationship with WSe_2. The thin Bragg peaks in radial scans in Fig. 3(b) [full widths at half maximum (FWHM) of 0.48° and 0.70°] indicate the large grain size and the uniformity of the lattice parameter. In Fig. 3(c), the mosaic spread (FWHM of 1.54°) is negligibly small, which confirms the perfect orientation of Cr_2Te_3 on WSe_2.

All the XRD data are summarized in Table I. Compared to bulk values of Cr_2Te_3 with $a = 6.812$ Å and $c = 12.07$ Å [46], we systematically found an in-plane compressive strain and a resulting out-of-plane expansion. We found similar lattice parameters regardless of the substrate underneath, although the mismatch between interatomic distances is very large (WSe_2: +19.1%/Gr: +56.3%/Bi_2Te_3: −10.8%). An in-plane compressive strain would be expected for Cr_2Te_3 deposited on WSe_2 and graphene, whereas an in-plane tensile strain would be expected for the growth on Bi_2Te_3. Moreover, we could not find any commensurable relationship between the in-plane lattice parameter of Cr_2Te_3 and that of the substrate. This was confirmed by *ab initio* calculations: the lattice

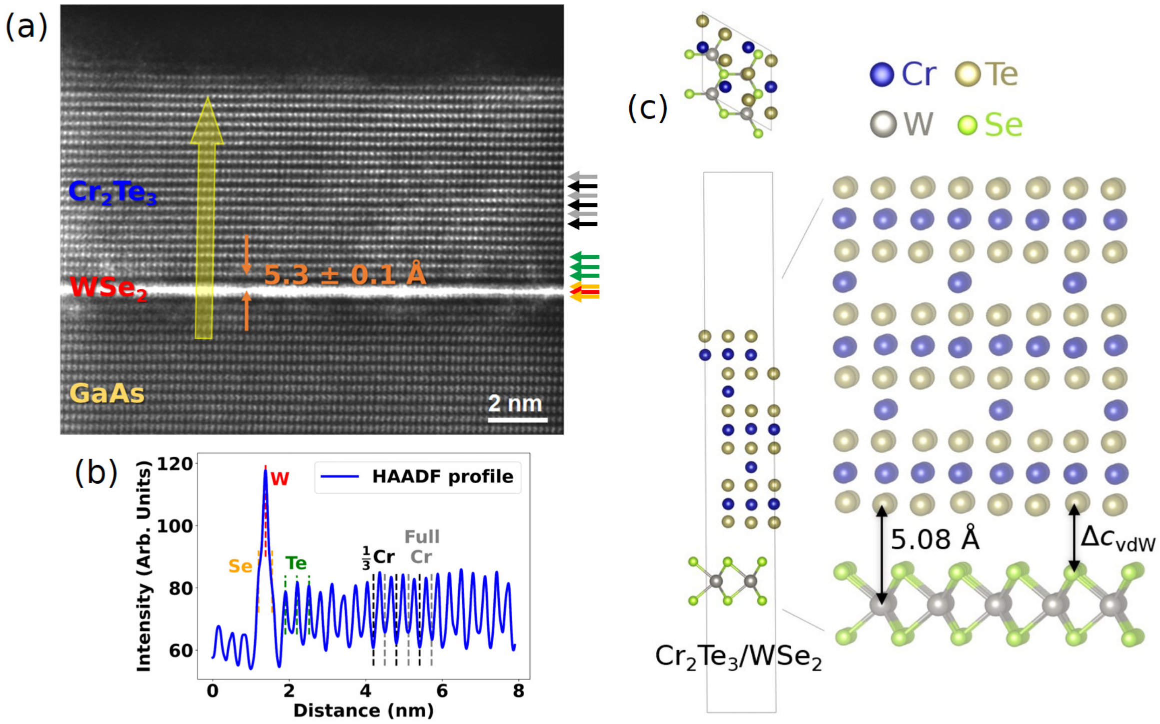

FIG. 2. (a) Low-pass-filtered HAADF-STEM image of five-layer Cr_2Te_3 grown on monolayer WSe_2 deposited on a GaAs(111)B surface. The van der Waals gap between the layers is shown to highlight the high quality of the interface. Arrows on the right side indicate the position of each atomic plane noted (by color) in the line profile. (b) Line profile along the c direction of the Cr_2Te_3 layers (yellow arrow) with intensity distinction between partially and fully occupied Cr planes [see crystal structure in (c)]. (c) A unit cell of the calculated Cr_2Te_3/WSe_2 heterostructure; in the interstitial planes, only 1/3 of the lattice sites are occupied by the intercalated Cr atoms. The *ab initio*-calculated W-Te distance is 5.08 Å.

parameter of the vdW heterostructure corresponds to that of bulk Cr_2Te_3 above 7 ML of Cr_2Te_3, as demonstrated for Cr_2Te_3/Gr (see the Supplemental Material, Fig. S2 [45]). We thus make a conclusion about the pure vdW interaction between Cr_2Te_3 and the substrate. The slight difference between lattice parameters might be due to the surface topography (presence of steps, terrace, etc.) and the microscopic structure of Cr_2Te_3 (grain size, grain boundaries, etc.).

However, the energy given to the system by annealing seems to be the driving force to control the final crystal structure since the lattice parameters for the samples on graphene and WSe_2 converge to the same values after annealing at 400 °C. The difference for Bi_2Te_3 is discussed in Fig. 6 below. In addition, layers grown on graphene exhibit a much larger mosaic spread even after annealing. The reason is probably the fact that the van der Waals interaction between Cr_2Te_3 and graphene is weaker than on the other 2D substrates. In that case, the crystal domains grow epitaxially on graphene, but because of this weaker interaction, they can rotate around this direction (when the nuclei are small) and be fixed in a position with slight angular deviation corresponding to some atomic coincidences, as shown by Vergnaud *et al.* [47].

The measured lattice parameters match well the *ab initio* calculations performed on ~5 nm thick freestanding films, which corresponds to the experimental thickness (see Fig. 4). In particular, for the Cr_2Te_3 films annealed on graphene and WSe_2 (samples 2 and 4), the experimental lattice parameters fall exactly on the theoretical curve, confirming a weak interaction between the film and the substrate. The case of Cr_2Te_3 grown on Bi_2Te_3 is discussed in Fig. 5.

In Table I, we also show the measured composition of some selected samples using RBS (see the Supplemental Material, Fig. S4 [45]) and find compositions very close to Cr_2Te_3. No measurement could be performed on GaAs substrates because Ga and As are heavier than chromium, causing the Cr signal peak to lie in the substrate background, preventing any determination of the Cr:Te ratio in these samples.

Raman spectroscopy was also performed before and after the growth of Cr_2Te_3 to control the quality and integrity of the 2D layers. Figure 3(d) depicts the Raman spectra of WSe_2/GaAs and Cr_2Te_3/WSe_2/GaAs. The width and position of WSe_2 peaks are preserved, indicating that the deposition of Cr_2Te_3 did not alter the WSe_2 layer. The reference signal of WSe_2/GaAs (green curve) was measured with a 532 nm laser instead of 633 nm used for the other samples, explaining the intensity differences. Similar observations have been made for the Cr_2Te_3/graphene heterostructure, as shown in Fig. S5 in the Supplemental Material [45].

Figure 5(a) shows the Raman spectra of $Cr_2Te_3/Bi_2Te_3/Al_2O_3$ at different stages of growth. We detected two characteristic peaks of Bi_2Te_3 at 101.8 and 133.5 cm^{-1}, which correspond to the E_g^2 and A_{1g}^2 vibrational modes and were also reported in [48]. After the deposition of five layers of Cr_2Te_3 at 300 °C, those peaks remained unchanged (the amplitude drop is explained by the partial absorption of the laser

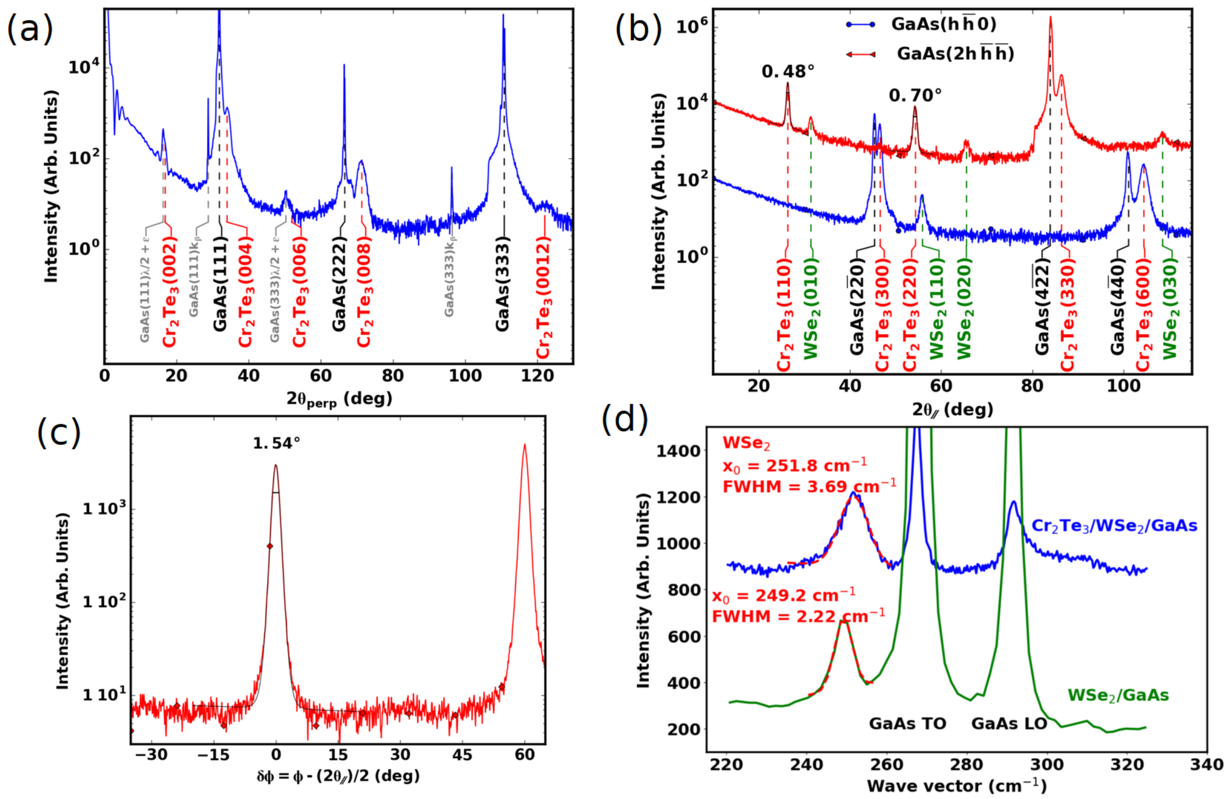

FIG. 3. Postgrowth characterization of the crystal structure of $Cr_2Te_3/WSe_2/GaAs$ (sample 2). (a) Out-of-plane $\Theta/2\Theta$ XRD scan shows, in addition to Cr_2Te_3 (00l) peaks (red), GaAs substrate peaks (black) with weak additional peaks due to spurious radiation not completely eliminated by the mirror and the $K\beta$ filter (gray). (b) In-plane radial XRD scans performed along the GaAs substrate $R = (h\bar{h}0)$ direction and $R + 30^\circ = (2h\bar{h}\bar{h})$ direction. These scans show the substrate peaks (black), WSe_2 (green), and Cr_2Te_3 peaks (red) labeled with their FWHM. (c) In-plane azimuthal XRD scan of the (300) peak measured within a range of 100° shows thin peaks with a FWHM of 1.54° separated by 60° corresponding to the sixfold symmetry of the crystal. (d) Raman spectra of WSe_2 before and after deposition of Cr_2Te_3.

fluence in the metallic Cr_2Te_3 layer). However, when the sample was annealed at 400 °C, the two characteristic peaks of Bi_2Te_3 disappeared. Indeed, x-ray diffraction measurements performed before and after annealing in Fig. 5(b) clearly show the disappearance of Bi_2Te_3 after thermal annealing. Finally, in Fig. 5(c), RBS measurements on the annealed sample show the absence of Bi in the heterostructure. We assume that Bi_2Te_3 was evaporated during annealing, leaving the Cr_2Te_3 film on the pristine sapphire substrate. We set the structural data of this sample (sample 6) in bold in Table I because Cr_2Te_3 stands directly on the sapphire substrate after annealing. Moreover, in this case, the substrate is no longer vdW, and defects might have been created in Cr_2Te_3 by evaporation of the Bi_2Te_3 layer underneath.

V. MAGNETIC PROPERTIES

Hysteresis loops were measured by SQUID magnetometry at 5 K and are displayed in Fig. 6. For all samples, the easy axis of magnetization was found along the *c* axis, and by integrating the difference in area between the out-of-plane and in-plane magnetization curves, the magnetic anisotropy energy (MAE) could be experimentally derived for all the samples.

TABLE I. Annealing temperature (all samples were grown at 300 °C) and structural parameters measured by x-ray diffraction and chemical composition from RBS, with *a* (*c*) being the in-plane (out-of-plane) lattice parameter and the radial width $\Delta\theta_{||}$ of the (300) diffraction peak and the mosaic spread $\Delta\phi$ measured on the same Bragg peak. The bold text indicates that Cr_2Te_3 stands directly on the sapphire substrate after annealing.

Sample	2D layer	Temperature (°C)	*a* (Å)	$\frac{a-a_{\mathrm{bulk}}}{a_{\mathrm{bulk}}}$	*c* (Å)	$\frac{c-c_{\mathrm{bulk}}}{c_{\mathrm{bulk}}}$	$\frac{c}{a}$	$\Delta\theta_{\|\|}$	$\Delta\phi$	Stoichiometry
1	WSe_2	300	6.731	−1.2%	12.44	+3.1%	1.848	1.00°	2.36°	
2	WSe_2	400	6.760	−0.76%	12.28	+1.7%	1.817	0.62°	1.54°	
3	graphene	300	6.754	−0.88%	12.18	+0.91%	1.804	0.72°	24.8°	$Cr_{1.88}Te_3$
4	graphene	400	6.758	−0.79%	12.30	+1.9%	1.820	0.60°	16.6°	
5	Bi_2Te_3	300	6.691	−1.8%	12.50	+3.6%	1.868	0.87°	2.77°	$Cr_{1.97}Te_3$
6	$\mathbf{Bi_2Te_3}$	**400**	**6.778**	−0.50%	**12.18**	**+0.91%**	**1.797**	**0.56°**	**1.28°**	$\mathbf{Cr_{2.07}Te_3}$

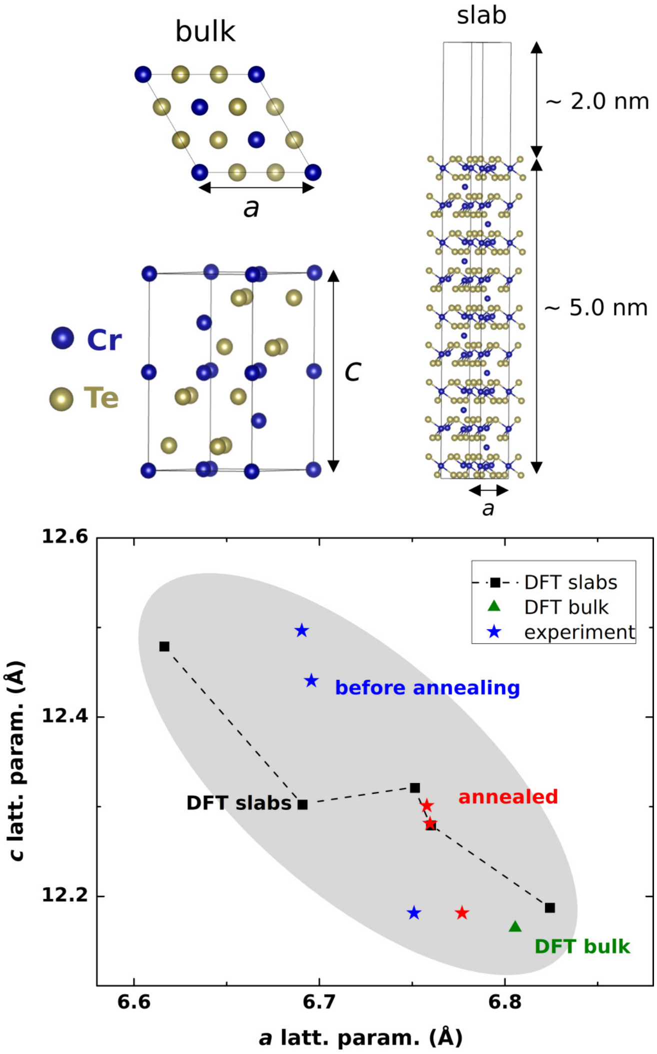

FIG. 4. Top: Cr_2Te_3 bulk crystal structure and a thin freestanding film constructed from it. The in-plane lattice parameter *a* was fixed at a range of values while the atomic positions were relaxed to obtain the out-of-plane lattice parameter *c*. Bottom: The calculated and experimental lattice parameters for freestanding slabs and for bulk structures. The measured values follow well the trend calculated for freestanding Cr_2Te_3 films.

The origin of ferromagnetism in our layers was confirmed by XMCD performed at the SOLEIL synchrotron radiation source. The energy spectra are shown in Fig. 7, and a hysteresis loop is displayed in Fig. S6 in the Supplemental Material [45]. A clear magnetic dichroism signal with a similar spectral shape was obtained for all three different substrates. This proves that the chemical environment of Cr atoms in Cr_2Te_3 films is essentially independent of the substrate. The lower magnetic moment for the sample on Bi_2Te_3/Al_2O_3 [Fig. 7(c)] is explained by a lower sample thickness (3 ML instead of 5 ML).

To better understand the magnetic properties, the magnetic anisotropy energy was calculated theoretically as a function of strain for bulk Cr_2Te_3 and is compared to experimental values in Fig. 8. The results reveal that the MAE is correlated with the strain of the layers. Overall, the trend and magnitude correspond well with experimental data. In particular, there is no sharp discontinuous change from positive to negative anisotropy values, as reported in [14]. However, the experimental data show larger PMA values compared to the theory. Since our calculations were performed in bulk Cr_2Te_3, we can attribute this shift to the presence of interfacial PMA at the Cr_2Te_3/substrate or Cr_2Te_3/AlO_x capping layer interfaces.

To determine the T_C of each annealed sample, we recorded the remanent magnetization after saturation at 5 T (with 5 K steps and no external field) as a function of temperature (Fig. 9). A value close to 180 K was found for the three substrates, demonstrating again the very weak interaction between Cr_2Te_3 and the vdW substrates. These results are very close to the bulk value of Cr_2Te_3 and to the values obtained in other similar studies on thin films [49,50]. We did not observe any increase of T_C in the thin limit as found by Wen *et al.* [14]. Here, we believe that T_C is fully determined by the 2:3 stoichiometry of the films, in agreement with Fujisawa *et al.* [12]. Finally, a lower remanent magnetization is observed for the sample grown on graphene. Indeed, the Cr_2Te_3 layers on graphene have a larger in-plane mosaicity, and therefore, we expect the grain boundaries to host more defects like point dislocations. These can act as nucleation centers (where the magnetic anisotropy is lowered) for magnetic domains and lead to a decrease in the magnetization at the remanence.

VI. MAGNETOTRANSPORT

To study the magnetotransport properties, we performed four-probe resistance measurements and found an increasing longitudinal resistivity of Cr_2Te_3 layers with temperature, indicating a metallic character (see the Supplemental Material, Fig. S8 [45]). The resistivity is of the order of 500 $\mu\Omega$ cm at 4 K. Figure 10(a) shows the Hall resistivity of 5 ML of Cr_2Te_3 deposited on WSe_2 (sample 2) as a function of the perpendicular magnetic field at different temperatures. For visibility, the ordinary Hall slope was subtracted, and a carrier density of 1.6×10^{15} holes/cm^2 was extracted at 50 K, compared to 7.0×10^{15} holes/cm^2 for 5 ML of Cr_2Te_3 directly deposited on sapphire (see the Supplemental Material, Fig. S9 [45]), indicating a charge transfer from the WSe_2 layer. The clear anomalous Hall signal confirmed the strong PMA of the ferromagnet.

The same measurements were performed for a sample grown on Bi_2Te_3 (sample 6) and annealed at 400 °C (resulting in Bi_2Te_3 evaporation), as shown in Fig. 10(b). The ordinary Hall slope was removed, and a carrier density of 4.5×10^{15} holes/cm^2 was extracted at 50 K. Since there is no charge transfer with sapphire, the difference in carrier density with Cr_2Te_3 directly grown on sapphire could be explained by the presence of defects at the interface introduced during the evaporation of the Bi_2Te_3 layer.

In Fig. 11(a), the anomalous Hall resistivity is extracted for the two samples on sapphire as a function of temperature. We observe in both cases a sign change of the anomalous Hall (AH) resistivity below the Curie temperature of 180 K. Similar observations were reported in [51,52]. The possible origin of this effect is discussed in the following as a consequence of the energy-dependent Berry phase of Cr_2Te_3.

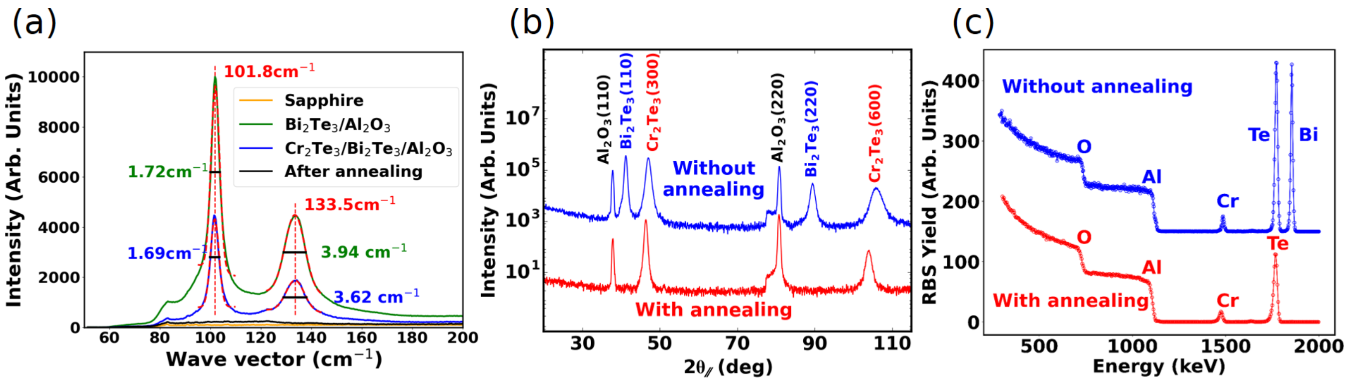

FIG. 5. Structural properties of Cr_2Te_3 on Bi_2Te_3/Al_2O_3. (a) Raman spectra of the sapphire substrate, Bi_2Te_3/sapphire, and Cr_2Te_3/Bi_2Te_3/sapphire with and without annealing. Positions and FWHM of Bi_2Te_3 peaks are indicated. (b) Radial x-ray diffraction spectra for $Cr_2Te_3/Bi_2Te_3/Al_2O_3$ without (blue) and after (red) annealing. (c) RBS of Cr_2Te_3 grown on Bi_2Te_3/Al_2O_3 without (blue) and with (red) annealing. No elemental Bi can be found after annealing.

In the temperature range of the AH resistivity sign reversal, a resonance of the Hall signal manifesting as peaks at the coercive fields can be observed. Figure 11(b) shows the Hall resistivity after subtraction of the ordinary and anomalous Hall effect (AHE) at two temperatures below the sign change and one above it (see the Supplemental Material, Fig. S10, for the details of the fit [45]). The bumps are enhanced when the temperature is closer to (but still lower than) the temperature of the sign change and disappear above it. The width of the bumps also decreases with temperature, which could be related to the shrinking of the coercive field. The physical origin of such an effect is still under debate. In a similar heterostructure, Chen *et al.* [20] interpreted it as the topological Hall effect, which would originate from the presence of magnetic skyrmions. Skyrmions nucleate during the magnetization reversal and give rise to an extra transverse transport channel, inducing a peak in the Hall resistivity. Imaging such spin textures was performed using Lorentz transmission electron microscopy for Cr_3Te_4 layers [53]. Nevertheless, another explanation of two anomalous Hall contributions with opposite signs was put forward by other groups [54]. The origin could be thickness variations, inhomogeneities in the film, or interface effects leading to the sign of the AHE being different [55,56]. In the case of Cr_2Te_3 these peaks appear close to the anomalous Hall resistivity sign change. If the thickness of the layer is not strictly constant over the Hall bar, some areas could have slightly different temperatures at which the anomalous Hall signal changes sign. In this case, for intermediate temperatures, two AHE components with opposite signs would, indeed, add up and could explain the observed behavior.

The sign reversal of the anomalous Hall effect observed experimentally can be elucidated by *ab initio* calculations. The

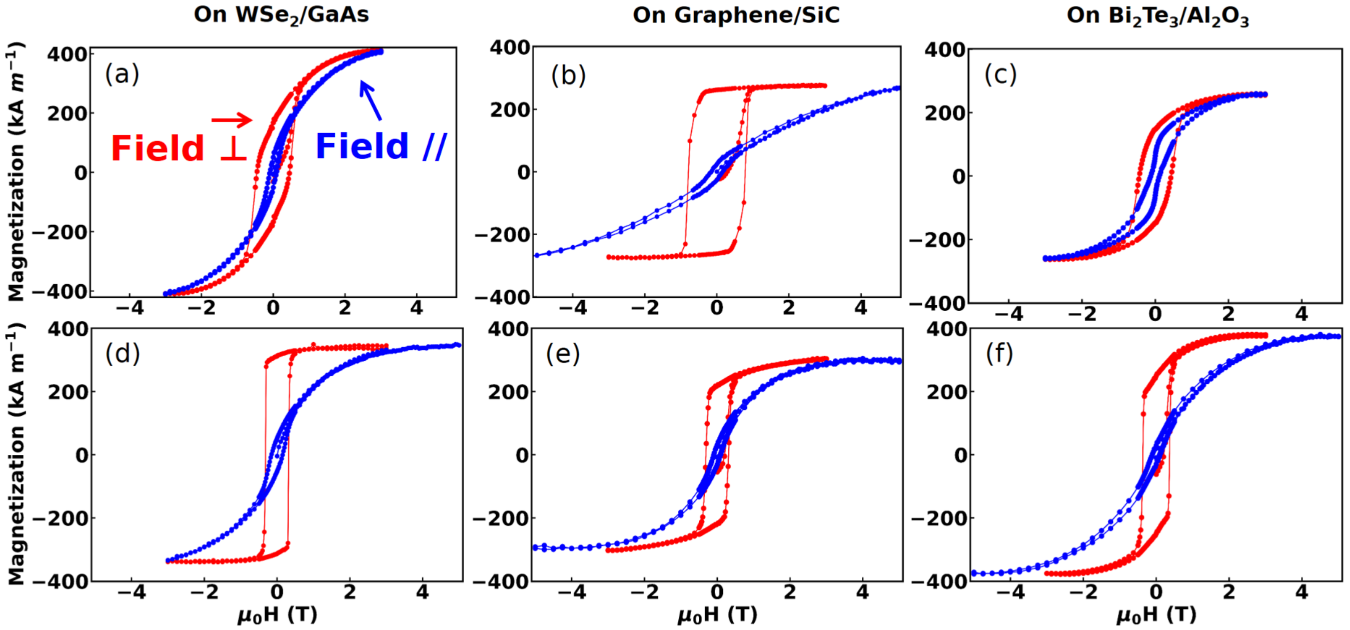

FIG. 6. SQUID hysteresis loops with out-of-plane (⊥) and in-plane (||) applied magnetic field measured at 5 K are plotted after the removal of the substrate diamagnetic contribution. Measurements on samples (a) 1, (b) 3, and (c) 5 (without annealing on $WSe_2/GaAs$, graphene/SiC, and Bi_2Te_3/Al_2O_3). (d)–(f) Same measurements as in (a)–(c), but on samples 2, 4, and 6 (annealed at 400 °C).

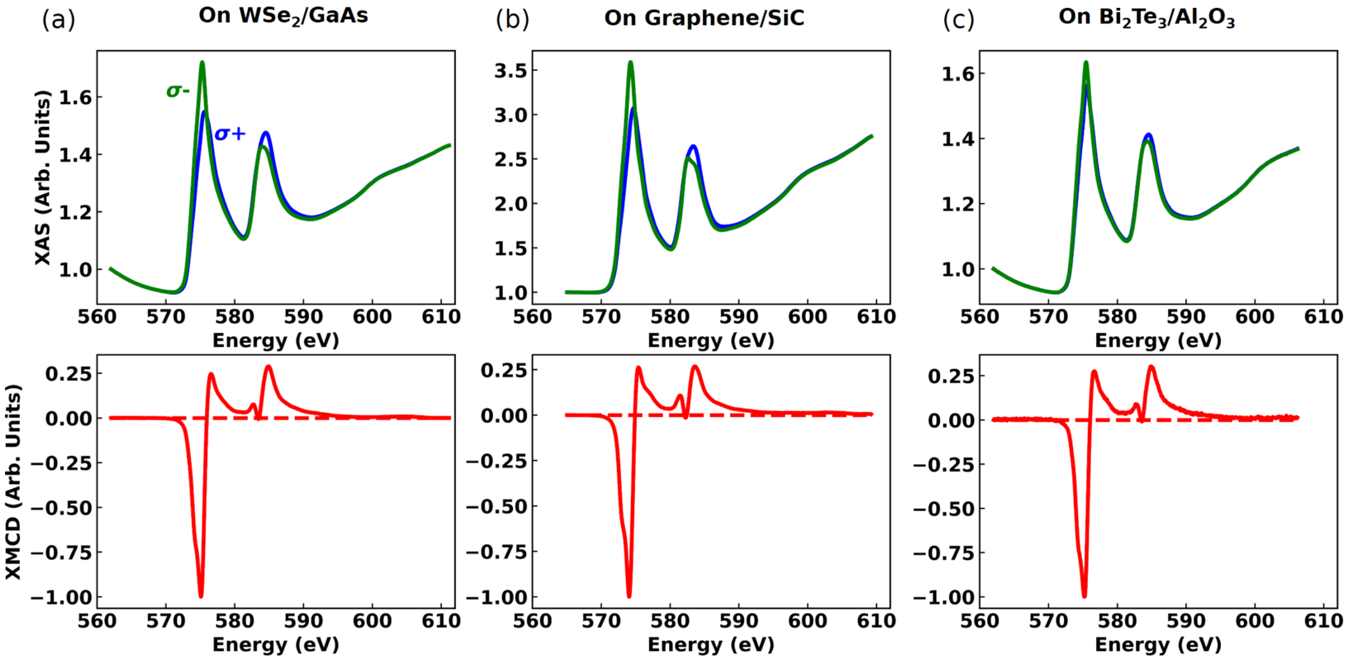

FIG. 7. X-ray absorption spectroscopy (XAS; top row) and x-ray magnetic circular dichroism (XMCD; bottom row) measurements performed on Cr_2Te_3 layers grown and annealed on (a) WSe_2 (sample 2), (b) graphene (sample 4), and (c) Bi_2Te_3 (sample 6).

longitudinal resistivity is in the range where contributions to the AHE from intrinsic and impurity scattering components coexist, while the intrinsic part remains significant [52]. We thus calculated the intrinsic contribution to AHE for bulk Cr_2Te_3 (see Sec. II). As shown in Fig. 12, it exhibits a clear sign reversal very close to E_F ($\sim\!-10$ meV). This is in contrast to previous calculations [22] in which the sign reversal occurs 330 meV above E_F. This difference is due to the inclusion of the vdW corrections in our DFT calculations (see the Supplemental Material, Fig. S11 [45]). We consider three different mechanisms influencing the value and sign of the anomalous Hall conductivity: (a) thermal broadening around the Fermi level (of the order of k_BT, i.e., 15 meV for $\Delta T = 180$ K), (b) charge transfer with the substrate (which we calculated was greatest on graphene, inducing a Fermi level shift of $\approx +50$ meV; see the Supplemental Material, Fig. S12 [45]), and (c) out-of-plane strain. All these effects change the system energy in a range compatible with the calculations in Fig. 12.

We believe that the strain dependence of σ_{AH}^{int} is at the origin of the change in sign of the AHE reported in Fig. 11(a). Anisotropic lattice expansion with temperature was reported for $Cr_{1+\delta}Te_2$ [57], which directly affects the AHE conductivity. To illustrate this qualitative argument, we choose in Fig. 12 two reasonable strain values in agreement with the structural data we obtained, keeping in mind that films in this work have c/a ranging between 1.797 and 1.868 (see Fig. 8). If the Fermi level of the sample lies in the red shaded area (between −8 and 0 meV), the evolution of c/a from

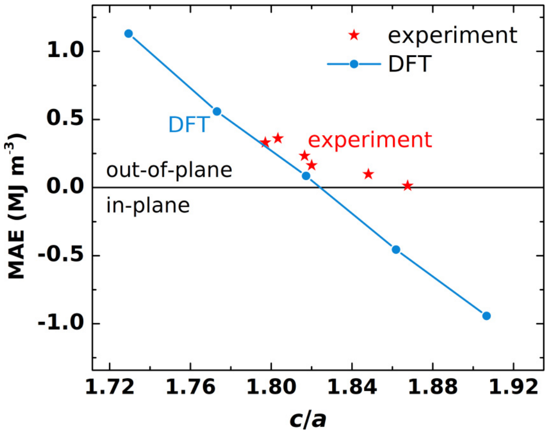

FIG. 8. Magnetic anisotropy energy of bulk Cr_2Te_3 as a function of strain compared for experiment and theory. It is a sum of the DFT-calculated magnetocrystalline energy and a demagnetizing energy contribution of -0.06 MJ/m^3 corresponding to the experimentally measured magnetization of $\approx$300 kA/m.

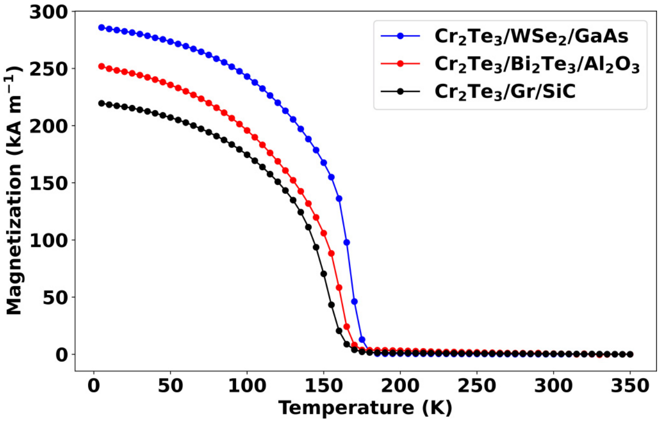

FIG. 9. Remanent magnetization of Cr_2Te_3 layers grown and annealed on WSe_2 (sample 2), graphene (sample 4), and Bi_2Te_3 (sample 6) as a function of temperature with no external field.

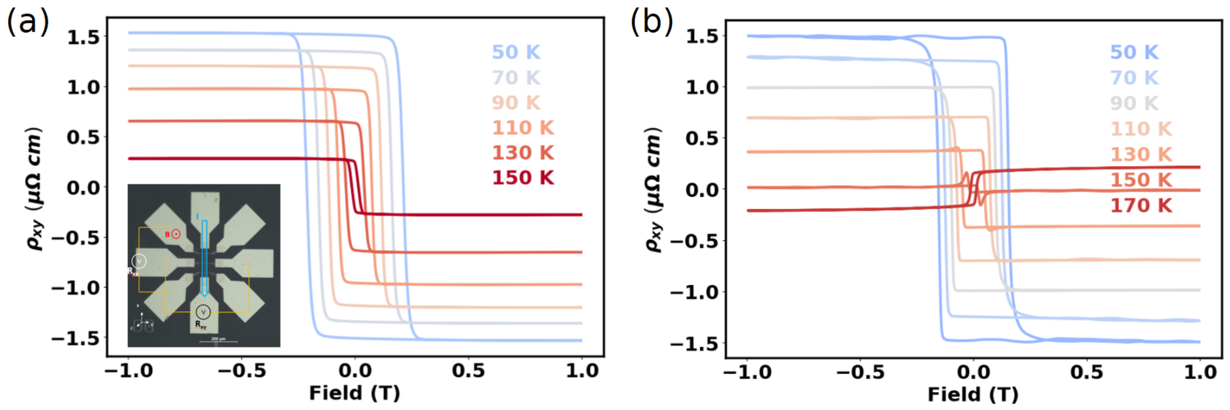

FIG. 10. (a) Temperature-dependent Hall resistivity of $Cr_2Te_3/WSe_2/GaAs$ (sample 2) after removal of the ordinary Hall slope with a magnetic field applied out of plane. Inset: An optical image of the Hall bar device processed by laser lithography with Ti(10nm)/Au(100nm) contacts. (b) Temperature-dependent Hall resistivity of $Cr_2Te_3/Bi_2Te_3/Al_2O_3$ (sample 6) after annealing (evaporation of Bi_2Te_3) and subtraction of the ordinary Hall slope.

1.79 to 1.82 with temperature will lead to a sign change of $\sigma_{\mathrm{AH}}^{\mathrm{int}}$.

Another effect that could influence this picture is the thermal broadening of the Fermi-Dirac distribution upon heating. However, we obtained a mostly linear dependence of $\sigma_{\mathrm{AH}}^{\mathrm{int}}$ on energy close to the Fermi level. When considering contributions above and below E_F, both would cancel out because the thermal broadening is symmetric. Finally, the role of the substrate also has to be accounted for. As shown experimentally, charge transfer with the 2D materials is observed and leads to a shift of the Fermi level. This explains why the effect is present for samples standing on sapphire and not for the one on WSe_2. Indeed, for sapphire, the Fermi level is the lowest (carrier density of 4.5×10^{15} holes/cm^2 and 7.0×10^{15} holes/cm^2), so we observe a sign change, whereas the Fermi level is shifted up for WSe_2 (1.6×10^{15} holes/cm^2) and the sign change is absent. This observation is in agreement with the fact that the sign change in *ab initio* calculations occurs for lower energies, as shown in Fig. 12.

Finally, in Fig. 13, we present magnetotransport measurements on five layers of Cr_2Te_3 grown on graphene/SiC (sample 3). Both layers are metallic and contribute to conduction. The Hall resistivity is plotted as a function of the applied perpendicular magnetic field at different temperatures. No anomalous Hall resistivity sign change is measurable below the Curie temperature. This observation is in good agreement with *ab initio* calculations since the extracted carrier density at 50 K, which is the lowest one (1.4×10^{14} holes/cm^2), corresponds to a Fermi level position shifted towards higher values. On top of the anomalous Hall contribution following the magnetization reversal at 0.5 T (at 50 K), another step close to 0.4 T is also present. This two-step signal behavior (absent in SQUID and XMCD measurements) vanishes progressively with an increase in temperature and disappears around 100 K, well below the Curie temperature. The origin of this effect needs to be investigated further and is out of the scope of the present work.

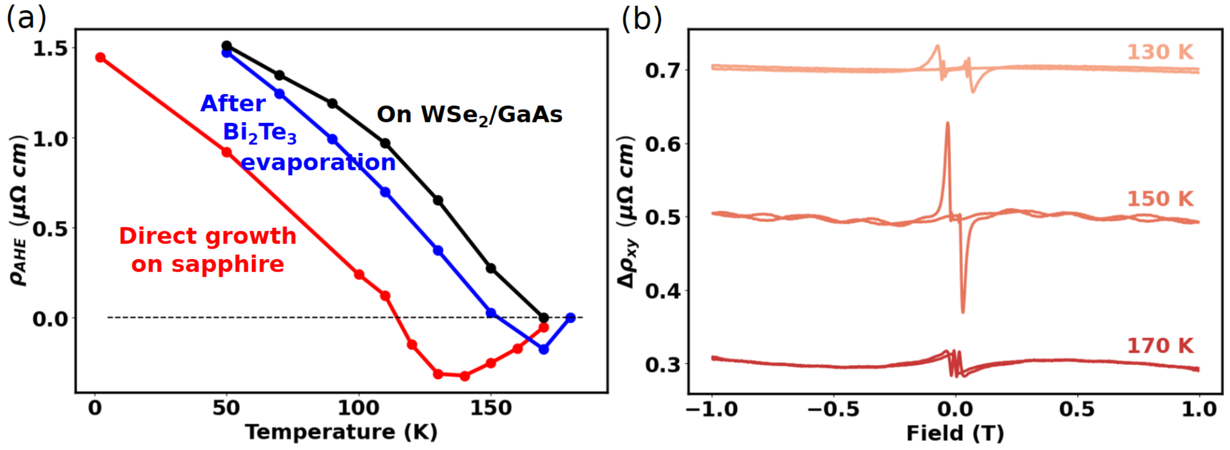

FIG. 11. (a) Anomalous Hall resistivity of Cr_2Te_3/Al_2O_3 as a function of temperature for direct growth on sapphire, after thermal removal of the Bi_2Te_3 layer and growth on WSe_2. (b) Hall resistivity of Cr_2Te_3 deposited on Bi_2Te_3 and annealed after subtracting the ordinary and anomalous Hall contributions. The curves are vertically shifted for clarity.

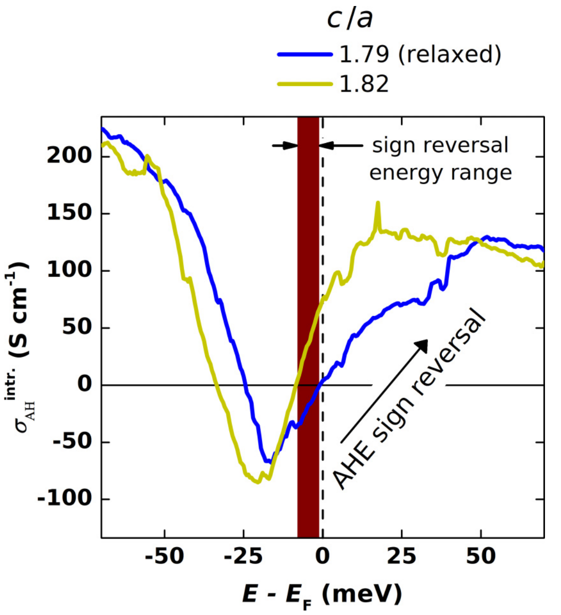

FIG. 12. Intrinsic anomalous Hall conductivity in bulk Cr_2Te_3 as a function of energy. A sign reversal occurs close to E_F. Two different strains (c/a ratios) are considered, in agreement with the experimental ones. Films with E_F within the red energy range will experience σ_{AH}^{int} sign reversal upon this possible strain change with temperature.

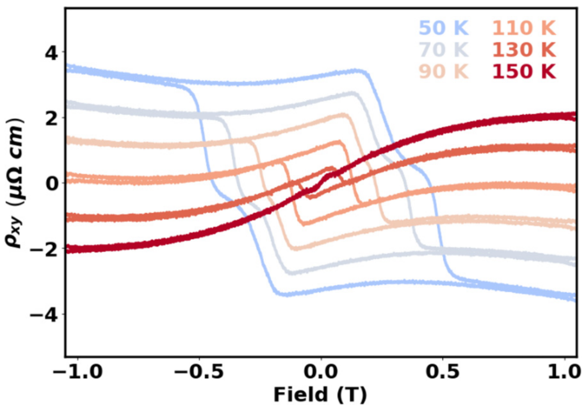

FIG. 13. Temperature-dependent Hall resistivity of Cr_2Te_3/graphene/SiC. An arbitrary slope of 4 $\mu\Omega$ cm/T has been subtracted for comparison with Fig. 10.

VII. CONCLUSION

In conclusion, we reported the vdW epitaxy of Cr_2Te_3 on three different 2D materials. We revealed the pristine interface and the preservation of the intrinsic properties of the underlying layers after the growth of the vdW ferromagnet. We demonstrated the freestanding character of Cr_2Te_3 layers grown on these 2D materials after an annealing step at 400 °C. In addition, the energy given to the system during the growth was identified as a way to control the crystal structure and tune the magnetic properties. We observed a correlation between the PMA energy of the system and the lattice parameters which was elucidated by *ab initio* calculations. Finally, we theoretically predicted a strain-sensitive sign change of the Berry phase very close to the Fermi level, explaining the measured sign change of the AHE with temperature. Charge transfer between the 2D layers and Cr_2Te_3 was shown to directly affect the temperature at which the AHE changes sign by shifting the Fermi level. To summarize, this system outputs highly tunable structural, magnetic, and electrical properties, which presents an important advantage for future spintronic applications.

ACKNOWLEDGMENTS

This project has received funding from the European Union's Horizon 2020 research and innovation program under Grant Agreement No. 800945 (NUMERICS–H2020-MSCA-COFUND-2017) and Grant Agreement No. 881603 (Graphene Flagship). We also acknowledge the French National Research Agency through the MAGICVALLEY project (Grant No. ANR-18-CE24-0007) and the ESR-Equipex+ 2D-MAG project (Grant No. ANR-21-ESRE-0025) on two-dimensional magnetic materials. We acknowledge the financial support from the ANR project ELMAX (Grant No. ANR-20-CE24-0015) and from the LANEF framework (Grant No. ANR-10-LABX-51-01) for support for mutualized infrastructure. This work was partly supported by the French RENATECH network. XMCD experiments were performed on the DEIMOS beamline at SOLEIL synchrotron, France (Proposal No. 20220542). We are grateful to the SOLEIL staff for smoothly running the facility.

---

[1] C. Gong, L. Li, Z. Li, H. Ji, A. Stern, Y. Xia, T. Cao, W. Bao, C. Wang, Y. Wang, Z. Q. Qiu, R. J. Cava, S. G. Louie, J. Xia, and X. Zhang, Discovery of intrinsic ferromagnetism in two-dimensional van der Waals crystals, Nature (London) **546**, 265 (2017).

[2] B. Huang, G. Clark, E. Navarro-Moratalla, D. R. Klein, R. Cheng, K. L. Seyler, D. Zhong, E. Schmidgall, M. A. McGuire, D. H. Cobden, W. Yao, D. Xiao, P. Jarillo-Herrero, and X. Xu, Layer-dependent ferromagnetism in a van der Waals crystal down to the monolayer limit, Nature (London) **546**, 270 (2017).

[3] Q. H. Wang *et al.*, The magnetic genome of two-dimensional van der Waals materials, ACS Nano **16**, 6960 (2022).

[4] A. C. Ferrari *et al.*, Science and technology roadmap for graphene, related two-dimensional crystals, and hybrid systems, Nanoscale **7**, 4598 (2015).

[5] H. Yang, S. O. Valenzuela, M. Chshiev, S. Couet, B. Dieny, B. Dlubak, A. Fert, K. Garello, M. Jamet, D.-E. Jeong, K. Lee, T. Lee, M.-B. Martin, G. S. Kar, P. Sénéor, H.-J. Shin, and S. Roche, Two-dimensional materials prospects for non-volatile spintronic memories, Nature (London) **606**, 663 (2022).

[6] C. Liu, H. Chen, S. Wang, Q. Liu, Y.-G. Jiang, D. W. Zhang, M. Liu, and P. Zhou, Two-dimensional materials for next-generation computing technologies, Nat. Nanotechnol. **15**, 545 (2020).

[7] B. Dieny and M. Chshiev, Perpendicular magnetic anisotropy at transition metal/oxide interfaces and applications, Rev. Mod. Phys. **89**, 025008 (2017).

[8] M. Ribeiro, G. Gentile, A. Marty, D. Dosenovic, H. Okuno, C. Vergnaud, J.-F. Jacquot, D. Jalabert, D. Longo, P. Ohresser, A. Hallal, M. Chshiev, O. Boulle, F. Bonell, and M. Jamet, Large-scale epitaxy of two-dimensional van der Waals room-temperature ferromagnet Fe_5GeTe_2, npj 2D Mater. Appl. **6**, 10 (2022).

[9] D. C. Freitas, R. Weht, A. Sulpice, G. Remenyi, P. Strobel, F. Gay, J. Marcus, and M. Núñez-Regueiro, Ferromagnetism in layered metastable $1T - CrTe_2$, J. Phys.: Condens. Matter **27**, 176002 (2015).

[10] A. Purbawati, J. Coraux, J. Vogel, A. Hadj-Azzem, N. Wu, N. Bendiab, D. Jegouso, J. Renard, L. Marty, V. Bouchiat, A. Sulpice, L. Aballe, M. Foerster, F. Genuzio, A. Locatelli, T. O. Menteş, Z. V. Han, X. Sun, M. Núñez-Regueiro, and N. Rougemaille, In-plane magnetic domains and Néel-like domain walls in thin flakes of the room temperature $CrTe_2$ van der Waals ferromagnet, ACS Appl. Mater. Interfaces **12**, 30702 (2020).

[11] X. Zhang, Q. Lu, W. Liu, W. Niu, J. Sun, J. Cook, M. Vaninger, P. F. Miceli, D. J. Singh, S.-W. Lian, T.-R. Chang, X. He, J. Du, L. He, R. Zhang, G. Bian, and Y. Xu, Room-temperature intrinsic ferromagnetism in epitaxial $CrTe_2$ ultrathin films, Nat. Commun. **12**, 2492 (2021).

[12] Y. Fujisawa, M. Pardo-Almanza, J. Garland, K. Yamagami, X. Zhu, X. Chen, K. Araki, T. Takeda, M. Kobayashi, Y. Takeda, C. H. Hsu, F. C. Chuang, R. Laskowski, K. H. Khoo, A. Soumyanarayanan, and Y. Okada, Tailoring magnetism in self-intercalated $Cr_{1+\delta}Te_2$ epitaxial films, Phys. Rev. Mater. **4**, 114001 (2020).

[13] J. Dijkstrat, H. H. Weitering'i, C. F. van Bruggen, C. Haast, and R. A. de Groot, Band-structure calculations, and magnetic and transport properties of ferromagnetic chromium tellurides (CrTe, Cr_3Te_4,Cr,Te,), J. Phys.: Condens. Matter **1**, 9141 (1989).

[14] Y. Wen, Z. Liu, Y. Zhang, C. Xia, B. Zhai, X. Zhang, G. Zhai, C. Shen, P. He, R. Cheng, L. Yin, Y. Yao, M. Getaye Sendeku, Z. Wang, X. Ye, C. Liu, C. Jiang, C. Shan, Y. Long, and J. He, Tunable room-temperature ferromagnetism in two-dimensional Cr_2Te_3, Nano Lett. **20**, 3130 (2020).

[15] H. Li, L. Wang, J. Chen, T. Yu, L. Zhou, Y. Qiu, H. He, F. Ye, I. K. Sou, and G. Wang, Molecular beam epitaxy grown Cr_2Te_3 thin films with tunable Curie temperatures for spintronic devices, ACS Appl. Nano Mater. **2**, 6809 (2019).

[16] J. Zhou, X. Song, J. Chai, N. L. M. Wong, X. Xu, Y. Jiang, Y. P. Feng, M. Yang, and S. Wang, Structure dependent and strain tunable magnetic ordering in ultrathin chromium telluride, J. Alloys Compd. **893**, 162223 (2022).

[17] Q.-Q. Li, S. Li, D. Wu, Z.-K. Ding, X.-H. Cao, L. Huang, H. Pan, B. Li, K.-Q. Chen, and X.-D. Duan, Magnetic properties manipulation of $CrTe_2$ bilayer through strain and self-intercalation, Appl. Phys. Lett. **119**, 162402 (2021).

[18] A. L. Coughlin, D. Xie, X. Zhan, Y. Yao, L. Deng, H. Hewa-Walpitage, T. Bontke, C.-W. Chu, Y. Li, J. Wang, H. A. Fertig, and S. Zhang, Van der Waals superstructure and twisting in self-intercalated magnet with near room-temperature perpendicular ferromagnetism, Nano Lett. **21**, 9517 (2021).

[19] K. Lasek, P. M. Coelho, P. Gargiani, M. Valvidares, K. Mohseni, H. L. Meyerheim, I. Kostanovskiy, K. Zberecki, and M. Batzill, Van der Waals epitaxy growth of 2D ferromagnetic $Cr(1+\delta)Te_2$ nanolayers with concentration-tunable magnetic anisotropy, Appl. Phys. Rev. **9**, 011409 (2022).

[20] J. Chen, L. Wang, M. Zhang, L. Zhou, R. Zhang, L. Jin, X. Wang, H. Qin, Y. Qiu, J. Mei, F. Ye, B. Xi, H. He, B. Li, and G. Wang, Evidence for magnetic skyrmions at the interface of ferromagnet/topological-insulator heterostructures, Nano Lett. **19**, 6144 (2019).

[21] J. Chen, L. Zhou, L. Wang, Z. Yan, X. Deng, J. Zhou, J.-W. Mei, Y. Qiu, B. Xi, X. Wang, H. He, and G. Wang, Conformal growth of Cr_2Te_3 on Bi_2Te_3 nanodots with a topological Hall effect, Cryst. Growth Des. **22**, 140 (2022).

[22] J. H. Jeon, H. R. Na, H. Kim, S. Lee, S. Song, J. Kim, S. Park, J. Kim, H. Noh, G. Kim, S.-K. Jerng, and S.-H. Chun, Emergent topological Hall effect from exchange coupling in ferromagnetic Cr_2Te_3/noncoplanar antiferromagnetic Cr_2Se_3 bilayers, ACS Nano, **16**, 8974 (2022).

[23] T. Pramanik, A. Roy, R. Dey, A. Rai, S. Guchhait, H. C. Movva, C.-C. Hsieh, and S. K. Banerjee, Angular dependence of magnetization reversal in epitaxial chromium telluride thin films with perpendicular magnetic anisotropy, J. Magn. Magn. Mater. **437**, 72 (2017).

[24] K. Ueno, K. Saiki, T. Shimada, and A. Koma, Epitaxial growth of transition metal dichalcogenides on cleaved faces of mica, J. Vac. Sci. Technol., A **8**, 68 (1990).

[25] F. S. Ohuchi, B. A. Parkinson, K. Ueno, and A. Koma, van der Waals epitaxial growth and characterization of $MoSe_2$ thin films on SnS_2, J. Appl. Phys. **68**, 2168 (1990).

[26] M. T. Dau, M. Gay, D. Di Felice, C. Vergnaud, A. Marty, C. Beigné, G. Renaud, O. Renault, P. Mallet, T. Le Quang, J.-Y. Veuillen, L. Huder, V. T. Renard, C. Chapelier, G. Zamborlini, M. Jugovac, V. Feyer, Y. J. Dappe, P. Pochet, and M. Jamet, Beyond van der Waals interaction: The case of $MoSe_2$ epitaxially grown on few-layer graphene, ACS Nano **12**, 2319 (2018).

[27] Y. J. Dappe, Y. Almadori, M. T. Dau, C. Vergnaud, M. Jamet, C. Paillet, T. Journot, B. Hyot, P. Pochet, and B. Grévin, Charge transfers and charged defects in WSe_2/graphene-SiC interfaces, Nanotechnology **31**, 255709 (2020).

[28] P. Ohresser, E. Otero, F. Choueikani, K. Chen, S. Stanescu, F. Deschamps, T. Moreno, F. Polack, B. Lagarde, J.-P. Daguerre, F. Marteau1, F. Scheurer, L. Joly, J.-P. Kappler, B. Muller, O. Bunau, and P. Sainctavit, Deimos: A beamline dedicated to dichroism measurements in the 350–2500 eV energy range, Rev. Sci. Instrum. **85**, 013106 (2014).

[29] G. Kresse and J. Hafner, *Ab initio* molecular dynamics for liquid metals, Phys. Rev. B **47**, 558 (1993).

[30] G. Kresse and J. Furthmüller, Efficiency of *ab-initio* total energy calculations for metals and semiconductors using a plane-wave basis set, Comput. Mater. Sci. **6**, 15 (1996).

[31] J. P. Perdew, K. Burke, and M. Ernzerhof, Generalized Gradient Approximation Made Simple, Phys. Rev. Lett. **77**, 3865 (1996).

[32] S. L. Dudarev, G. A. Botton, S. Y. Savrasov, C. J. Humphreys, and A. P. Sutton, Electron-energy-loss spectra and the structural stability of nickel oxide: An LSDA + U study, Phys. Rev. B **57**, 1505 (1998).

[33] S. Grimme, J. Antony, S. Ehrlich, and H. Krieg, A consistent and accurate *ab initio* parametrization of density functional dispersion correction (DFT-D) for the 94 elements H-Pu, J. Chem. Phys. **132**, 154104 (2010).

[34] S. Grimme, S. Ehrlich, and L. Goerigk, Effect of the damping function in dispersion corrected density functional theory, J. Comput. Chem. **32**, 1456 (2011).

[35] K. Choudhary, K. F. Garrity, S. T. Hartman, G. Pilania, and F. Tavazza, Efficient computational design of 2D van der Waals heterostructures: Band-alignment, lattice-mismatch, web-app generation and machine-learning, arXiv:2004.03025.

[36] A. Hallal, B. Dieny, and M. Chshiev, Impurity-induced enhancement of perpendicular magnetic anisotropy in Fe/MgO tunnel junctions, Phys. Rev. B **90**, 064422 (2014).

[37] X. Wang, J. R. Yates, I. Souza, and D. Vanderbilt, *Ab initio* calculation of the anomalous Hall conductivity by Wannier interpolation, Phys. Rev. B **74**, 195118 (2006).

[38] A. A. Mostofi, J. R. Yates, G. Pizzi, Y.-S. Lee, I. Souza, D. Vanderbilt, and N. Marzari, An updated version of wannier90: A tool for obtaining maximally-localised Wannier functions, Comput. Phys. Commun. **185**, 2309 (2014).

[39] S. S. Tsirkin, High performance Wannier interpolation of Berry curvature and related quantities with WannierBerri code, npj Comput. Mater. **7**, 33 (2021).

[40] D. Destraz, L. Das, S. S. Tsirkin, Y. Xu, T. Neupert, J. Chang, A. Schilling, A. G. Grushin, J. Kohlbrecher, L. Keller, P. Puphal, E. Pomjakushina, and J. S. White, Magnetism and anomalous transport in the Weyl semimetal PrAlGe: Possible route to axial gauge fields, npj Quantum Mater. **5**, 5 (2020).

[41] A. Ouerghi, M. G. Silly, M. Marangolo, C. Mathieu, M. Eddrief, M. Picher, F. Sirotti, S. El Moussaoui, and R. Belkhou, Large-area and high-quality epitaxial graphene on off-axis SiC wafers, ACS Nano **6**, 6075 (2012).

[42] E. Pallecchi, F. Lafont, V. Cavaliere, F. Schopfer, D. Mailly, W. Poirier, and A. Ouerghi, High electron mobility in epitaxial graphene on 4H-SiC(0001) via post-growth annealing under hydrogen, Sci. Rep. **4**, 4558 (2014).

[43] B. Kumar, M. Baraket, M. Paillet, J.-R. Huntzinger, A. Tiberj, A. Jansen, L. Vila, M. Cubuku, C. Vergnaud, M. Jamet, G. Lapertot, D. Rouchon, A.-A. Zahab, J.-L. Sauvajol, L. Dubois, F. Lefloch, and F. Duclairoir, Growth protocols and characterization of epitaxial graphene on SiC elaborated in a graphite enclosure, Phys. E **75**, 7 (2016).

[44] D. Pierucci, A. Mahmoudi, M. Silly, F. Bisti, F. Oehler, G. Patriarche, F. Bonell, A. Marty, C. Vergnaud, M. Jamet, H. Boukari, E. Lhuillier, M. Pala, and A. Ouerghi, Evidence for highly *p*-type doping and type II band alignment in large scale monolayer WSe_2/Se-terminated GaAs heterojunction grown by molecular beam epitaxy, Nanoscale **14**, 5859 (2022).

[45] See Supplemental Material at http://link.aps.org/supplemental/10.1103/PhysRevMaterials.7.054005 for RHEED images on two different 2D materials (the third one is in the main text), the calculated lattice parameter of Cr_2Te_3 as a function of thickness, the atoms at the termination of Cr_2Te_3 layers, the measured stoichiometry by Rutherford backscattering, a hysteresis loop measured by XMCD, the calculated magnetic moment of each atom at the interface between Cr_2Te_3 and 2D materials, the temperature-dependent resistivity of Cr_2Te_3, Hall measurements of Cr_2Te_3 on sapphire, details on the fitting of the ordinary and anomalous Hall effects, and the strain-dependent intrinsic anomalous Hall contribution and charge transfer between Cr_2Te_3 and 2D materials. The Supplemental Material also contains Refs. [58–61].

[46] A. F. Andresen, E. Zeppezauer, T. Boive, B. Nordström, and C. Brändén, Magnetic structure of Cr_2Te_3, Cr_3Te_4, and Cr_5Te_6, Acta Chem. Scand. **24**, 3495 (1970).

[47] C. Vergnaud, M.-T. Dau, B. Grévin, C. Licitra, A. Marty, H. Okuno, and M. Jamet, New approach for the molecular beam epitaxy growth of scalable WSe_2 monolayers, Nanotechnology **31**, 255602 (2020).

[48] C. Wang, X. Zhu, L. Nilsson, J. Wen, G. Wang, X. Shan, Q. Zhang, S. Zhang, J. Jia, and Q. Xue, In situ Raman spectroscopy of topological insulator Bi_2Te_3 films with varying thickness, Nano Res. **6**, 688 (2013).

[49] A. Roy, S. Guchhait, R. Dey, T. Pramanik, C.-C. Hsieh, A. Rai, and S. K. Banerjee, Perpendicular magnetic anisotropy and spin glass-like behavior in molecular beam epitaxy grown chromium telluride thin films, ACS Nano **9**, 3772 (2015).

[50] N. Figueiredo-Prestes, P. Tsipas, S. Krishnia, P. Pappas, J. Peiro, S. Fragkos, V. Zatko, A. Lintzeris, B. Dlubak, S. Chaitoglou, M. Heuken, N. Reyren, H. Jaffrès, P. Seneor, A. Dimoulas, and J.-M. George, Large Fieldlike Spin-Orbit Torque and Magnetization Manipulation in a Fully Epitaxial van der Waals Two-Dimensional-Ferromagnet/Topological-Insulator Heterostructure Grown by Molecular-Beam Epitaxy, Phys. Rev. Appl. **19**, 014012 (2023).

[51] H. Chi *et al.*, Strain-tunable Berry curvature in quasi-two-dimensional chromium telluride, arXiv:2207.02318.

[52] Y. Fujisawa, M. Pardo-Almanza, C.-H. Hsu, A. Mohamed, K. Yamagami, A. Krishnadas, F. C. Chuang, K. H. Khoo, J. Zang, A. Soumyanarayanan, and Y. Okada, Widely tunable berry curvature in the magnetic semimetal $Cr_{1+\delta}Te_2$, Adv. Mater. **35**, 2207121 (2023).

[53] C. Zhang, C. Liu, J. Zhang, Y. Yuan, Y. Wen, Y. Li, D. Zheng, Q. Zhang, Z. Hou, G. Yin, K. Liu, Y. Peng, and X.-X. Zhang, Room-temperature magnetic skyrmions and large topological Hall effect in chromium telluride engineered by self-intercalation, Adv. Mater. **35**, 2205967 (2022).

[54] L. Tai, B. Dai, J. Li, H. Huang, S. K. Chong, K. L. Wong, H. Zhang, P. Zhang, P. Deng, C. Eckberg, G. Qiu, H. He, D. Wu, S. Xu, A. Davydov, R. Wu, and K. L. Wang, Distinguishing the two-component anomalous Hall effect from the topological hall effect, ACS Nano **16**, 17336 (2022).

[55] L. Wang, Q. Feng, H. G. Lee, E. K. Ko, Q. Lu, and T. W. Noh, Controllable thickness inhomogeneity and Berry curvature engineering of anomalous Hall effect in $SrRuO_3$ ultrathin films, Nano Lett. **20**, 2468 (2020).

[56] G. Kimbell, C. Kim, W. Wu, M. Cuoco, and J. W. A. Robinson, Challenges in identifying chiral spin textures via the topological Hall effect, Commun. Mater. **3**, 19 (2022).

[57] C. Li, K. Liu, D. Jiang, C. Jin, T. Pei, T. Wen, B. Yue, and Y. Wang, Diverse thermal expansion behaviors in ferromagnetic Cr1-dTe with NiAs-type, defective structures, Inorg. Chem. **61**, 14641 (2022).

[58] K. Lasek, P. M. Coelho, K. Zberecki, Y. Xin, S. K. Kolekar, J. Li, and M. Batzill, Molecular beam epitaxy of transition metal (Ti-, V-, and Cr-) tellurides: From monolayer ditellurides to multilayer self-intercalation compounds, ACS Nano **14**, 8473 (2020).

[59] M. Bian, A. N. Kamenskii, M. Han, W. Li, S. Wei, X. Tian, D. B. Eason, F. Sun, K. He, H. Hui, F. Yao, R. Sabirianov, J. P.

Bird, C. Yang, J. Miao, J. Lin, S. A. Crooker, Y. Hou, and H. Zeng, Covalent 2D Cr_2Te_3 ferromagnet, Mater. Res. Lett. **9**, 205 (2021).

[60] Y. Y. Wang, Z. H. Ni, T. Yu, Z. X. Shen, H. M. Wang, Y. H. Wu, W. Chen, and A. T. Shen Wee, Raman studies of monolayer graphene: The substrate effect, J. Phys. Chem. C **112**, 10637 (2008).

[61] Y. Kubota, Y. Okamoto, T. Kanematsu, T. Yajima, D. Hirai, and K. Takenaka, Large magnetic-field-induced strains in sintered chromium tellurides, Appl. Phys. Lett. **122**, 042404 (2023).